Electrochemical-thermal P2D aging model of a $LiCoO_2$/graphite cell: capacity fade simulations

A. Lamorgese[a,*], R. Mauri[b], B. Tellini[a]

[a] *DESTEC, Università di Pisa, Largo Lazzarino 1, 56122 Pisa, Italy*

[b] *DICI, Università di Pisa, Largo Lazzarino 1, 56122 Pisa, Italy*

Abstract

We simulate a simple model of aging in a lithium-ion cell that accounts for growth of a passivation film on the negative electrode, on top of an electrochemical-thermal pseudo-two-dimensional (P2D) description of "ideal" (i.e., ignoring aging effects) cell dynamics, using a finite-volume Matlab code. Capacity fade is assessed by evaluating at each instant in time the loss of cyclable lithium ions, which follows as a consequence of a single irreversible electrolyte decomposition reaction in the aging model. Assuming reasonable values for the side reaction rate and SEI film conductivity, we show an estimated 2.5% capacity loss after 1600 cycles at 1C. We also find a growth rate of about 0.64 nm/hr at 1C for the SEI film on the negative electrode, in a linear growth regime obtained by neglecting any diffusive transport limitations during new SEI formation. In addition, we show that for an "ideal" cell under cyclic loading conditions its energy dissipation (per cycle) is constant as a function of cycle number, while that same quantity keeps increasing with cycle number for an aging cell. Finally, we discuss the influence of the aging model as it affects surface cell temperature as a function of a (convective) heat transfer coefficient. Specifically, for values of h larger than about $1\,\mathrm{W/(m^2\,K)}$ we find essentially no effect of the aging model on surface cell temperature, which remains equal for all time to the surrounding ambient temperature. For smaller values of h, however, we find surface cell temperatures that are systematically larger than their "ideal" cell counterparts, with a strictly monotonic (increasing) behavior of the steady-state surface cell temperature as a function of the (reciprocal) heat transfer coefficient.

*Email: andrea.lamorgese@unipi.it.

Keywords: Lithium-ion battery; Eletrochemical-thermal model; Aging; SEI layer growth; Capacity fade; Charge-discharge cycles; Pseudo-two-dimensional model

1. Introduction

We present results of numerical simulations of a simple model of aging in a $LiCoO_2$/graphite cell, built on top of a pseudo-two-dimensional (P2D) electrochemical-thermal description of lithium-ion cell dynamics, as an intermediate step towards the verification and validation of the numerical code used to perform the simulations. The work reported herein is motivated by the need to establish a simulation and modeling capability for investigating predictive models of aging in a lithium-ion cell, in connection with a parallel experimental campaign towards the optimal design (with special attention paid to safety aspects) of a lithium-ion battery pack for small boats or ferries.

In general, since the performance of a lithium-ion battery declines over time as a consequence of a variety of aging processes, the main objective of modeling battery aging is to predict the fade of battery performance (in particular, its state of health) over a time frame typical of the targeted application. In its simplest form, the aging model would merely consist of an empirical correlation for cell capacity and internal resistance as a function of time, involving additional factors such as, e.g., current density, state of charge, etc. Then, a state-of-health prediction results from an empirical extrapolation of the correlation over time. Improved predictions could be obtained based on a more in-depth analysis, involving a performance model of the battery, wherein input parameters are updated to match the fade of cell performance over the course of an aging experiment. Now, performance models can range from fully empirical models (e.g., artificial neural networks) to semi-empirical models (such as, e.g., equivalent circuit models), all the way to physics-based models. This last category of models relies on the underlying physical phenomena (e.g., mass transport and electrochemical kinetics) taking place within a battery. In particular, using a physics-based model for analyzing battery performace allows one to describe aging phenomena on top of the original governing equations for the performance model, thereby turning it into a physics-based aging model [1, 2, 3, 4, 5]. This

is the most sophisticated approach to aging prediction, because it entails no additional empirical extrapolations. However, it also involves a heavy burden on the modeling side, since a thorough analysis of all cell components is required to derive an adequate physical description of the relevant aging phenomena. As is well known, aging mechanisms in lithium-ion batteries can be either mechanical or chemical and may depend on parameters such as cathode and anode materials, preparation methods, electrolyte composition [6], and battery working conditions. As a rule, battery aging produces two main effects: capacity fade and impedance rise [7]. In fact, a loss of cell performance results from various chemical mechanisms, which also depend on the electrode materials. Briefly, the main consequences of such mechanisms are as follows: (i) A passivation layer forms around the negative electrode (assuming graphite as the active material at the negative electrode) also known as the solid/electrolyte interphase (SEI) layer, and its growth leads to an impedance rise there; (ii) the SEI layer continues to grow at the negative (graphitic) electrode, with an attendant loss of cyclable lithium ions leading to capacity fade, as a result of electrolyte reduction and/or changes in the oxide surface structure [8]; (iii) the formation and growth of the SEI film leads to a gradual contact loss within the composite negative electrode and thus increases the impedance in the cell [9]; (iv) a loss of active electrode materials occurs, involving materials dissolution, structural degradation, particle isolation, and electrode decomposition [10]. Summarizing, battery aging mainly arises as a consequence of (i) loss of lithium inventory (LLI), (ii) loss of active material (LAM), and (iii) increase in resistance [11]. In fact, it should also be acknowledged that the causes of LLI can be traced not only to a thickening of the SEI film caused by electrolyte decomposition reactions, but also to new SEI formation resulting from fatigue crack propagation at the negative electrode under cyclic loading conditions, as well as additional SEI formation caused by lithium plating at the negative electrode during charging.

Although the very existence of an SEI layer is conducive to preventing undesired reduction/oxidation of electrolyte and electrodes [12], it also turns out that SEI film growth due to electrolyte decomposition is the primary cause of electrode materials aging [13]. In fact, although a large number of reduction reactions can lead to the deposition of solid products at the negative electrode,

herein we consider a simple model of aging, which is based on the assumption that there is a single additional irreversible side reaction that consumes the solvent species and lithium ions at a graphitic negative electrode, forming compounds such as Li_2CO_3, LiF, Li_2O, and so forth, depending on the nature of the solvent. Previous studies of SEI layer formation on lithiated graphite have shown that there is probably a significant porosity associated with the SEI layer, which makes it reasonable to assume that the SEI layer continues to grow as the solvent diffuses through the layer during charging [14, 15, 16, 17]. The assumption that the SEI layer forms during charging is also supported by recent experimental work [14], showing that the intercalation of lithium into a graphitic particle at the negative electrode leads to an increase in the lattice volume, thereby stretching the SEI layer and causing it to fracture and expose more of the negative electrode to the electrolyte, which in turn fuels the side reaction, leading to sustained growth of the SEI layer. Now, although a number of SEI film growth models have been published in the literature to date [5, 4, 18], herein we restrict our attention to a simple, kinetics-driven SEI film growth model [4], meaning that any diffusive transport limitations are ignored. In what follows, we rely on the same assumptions as in the original Ramadass et al. [4] model: (i) The main side reaction is due to the reduction of an organic solvent, expressed as $\mathrm{S} + 2\mathrm{Li}^+ + 2\mathrm{e}^- \rightarrow \mathrm{P}$, with S standing for the solvent, while P refers to the product formed in the side reaction; (ii) the reaction occurs only during charging of the cell; (iii) the products formed are a mixture of different species, resulting in an averaged molecular mass and density for describing growth of the SEI film; (iv) the side reaction is assumed to be irreversible and its reference equilibrium potential is assumed to be $U_s^{ref} = 0.4\,\mathrm{V}$ vs. $\mathrm{Li/Li}^+$ [4, 19, 20]; (v) lithium plating during charging is altogether neglected. Following Ramadass et al. [4], we incorporate the SEI layer growth model above on top of a P2D description of "ideal" (i.e., neglecting aging phenomena) cell dynamics [21, 22], which relies on a concentrated solution model of the electrolyte [23, 24, 25, 26], while assuming porous electrode theory for the electrodes [27, 28, 29]. Furthermore, the electrochemical (P2D) model considered herein is coupled to a macroscale energy balance equation (in 1D) that allows for the temperature dependence of material properties such as, e.g., open-circuit potentials and lithium-ion diffusivities and

conductivities, and, in particular, of the side reaction rate, since a consideration of temperature effects is mandatory towards the accurate modeling of aging effects [30, 31]. Even though the resulting 1D model is sometimes sufficient for simulating the thermal behavior of a single cell, this approach has significant limitations when applied to large format cells, modules, or for describing the thermal influence of current collector tabs. Recent work in this area involves coupling the P2D equations to a 3D thermal model [32, 33, 34, 35, 36, 37, 38].

The remainder of this paper is laid out as follows. Since the governing equations for a P2D description of lithium-ion cell dynamics are well known and have been reviewed in the literature many times [39, 40, 41, 42, 43, 44], below we are going to briefly introduce the P2D system of equations, followed by a more detailed discussion of the aging and thermal models employed for calculating the results reported herein. (For clarity as well as for emphasizing the micro- and macro-scale components in the electrochemical-thermal P2D system of equations, the reader can find a detailed derivation of the governing equation system employed herein in a companion *Data in Brief* paper [45].) Subsequently, we are going to present a quick summary of relevant numerical methods before we show the results (in Sect. 4) of numerical simulations with and without aging effect of the same $LiCoO_2$/graphite cell as presented by Cai and White [46]. Finally, in Section 5 a few conclusions are drawn.

2. Electrochemical-thermal P2D aging model

Doyle et al. [21, 22, 47, 48, 49, 41] established the P2D approach to lithium-ion cell dynamics, consisting in a macroscale description of charge and species transport in the solid and electrolyte phases in a porous electrode (and in the electrolyte phase in the separator) wherein all time-dependent fields (i.e., lithium-ion species concentrations and electrical potentials) are assumed to depend on a single spatial coordinate in a direction (x) across the cell thickness. In addition, a radial coordinate (a.k.a. the pseudo dimension) is used in the conservation equation for a solid intercalant species (enforced on the microscale) to specify a radial point inside an active solid particle presumed to reside at some spatial location (x). In other words, the (isothermal) P2D model expresses species and charge conservation applicable to both host material (subscript s)

and electrolyte (subscript e) phases [22]:

$$\frac{\partial(\varepsilon_e c_e)}{\partial t} = \frac{\partial}{\partial x}\left[D_e^{\mathit{eff}}\frac{\partial c_e}{\partial x}\right] + a_s(1-t_+^0)(j_i + j_s) \tag{1}$$

$$\frac{\partial c_s}{\partial t} = \frac{1}{r^2}\frac{\partial}{\partial r}\left[r^2 D_s^{\mathit{eff}}\frac{\partial c_s}{\partial r}\right] \tag{2}$$

$$-a_s F(j_i + j_s) = \frac{\partial}{\partial x}\left[\kappa^{\mathit{eff}}\frac{\partial \phi_e}{\partial x}\right] + \frac{\partial}{\partial x}\left[\kappa_D^{\mathit{eff}}\frac{\partial \ln c_e}{\partial x}\right] \tag{3}$$

$$a_s F(j_i + j_s) = \frac{\partial}{\partial x}\left[\sigma^{\mathit{eff}}\frac{\partial \phi_s}{\partial x}\right] \tag{4}$$

Here, c_s and c_e denote the solid intercalant species concentration and lithium-ion concentration in the electrolyte, respectively; similarly, ϕ_s and ϕ_e indicate the electrostatic potential in both the solid and electrolyte phases, while t_+^0 is the cation transference number (with respect to the solvent) in the electrolyte (F being Faraday's constant). As can be seen, the species and charge conservation equations above are coupled through the total current current density $F(j_i+j_s)$, with j_i and j_s denoting the intercalation and side reaction molar fluxes (herein j_s is assumed to exist only at the negative electrode during charging). The former is usually modeled via a Butler-Volmer kinetic relation:

$$j_i = \frac{i_0}{F}\left[\exp\left(\frac{F\eta}{2RT}\right) - \exp\left(-\frac{F\eta}{2RT}\right)\right] \tag{5}$$

where the local overpotential is defined as $\eta = \phi_s - \phi_e - U$, with U denoting the open-circuit potential (OCP) of a particular half-cell reaction. The OCP is in fact temperature-dependent and also a function of $c_{s,e}$, with $c_{s,e}$ denoting the surface concentration of intercalated lithium into an active particle at its solid/electrolyte interface. In anticipation of the electrochemical/thermal coupling addressed below, we note that a temperature-dependent OCP is usually represented based on a first-order Taylor expansion, i.e., $U = U_{ref} + (T - T_{ref})\,\frac{\partial U}{\partial T}\big|_{ref}$ (with subscript *ref* denoting in our case a reference uniform temperature of 298.15 K). Hence, to be able to calculate the OCP as a function of temperature and $\theta \equiv c_{s,e}/c_{s,max}$, we will have to employ model expressions for the entropy coefficients $\partial U/\partial T|_{ref}$ as a function of θ [50, 51, 52, 53]. Similarly, the exchange current density is a function of the intercalant species surface concentration:

$$\frac{i_0}{F} = k_0\left[c_e(c_{s,max} - c_{s,e})c_{s,e}\right]^{1/2} \tag{6}$$

where $c_{s,max}$ is the maximum stochiometric molar density of solid-phase intercalant. Since Eqs. (1), (3), and (4) in fact represent volume-averaged statements of species and charge conservation in a porous electrode (and in the electrolyte phase in a porous separator), the relevant effective solid and electrolyte transport properties (i.e., diffusivities D_e^{eff} and conductivities κ^{eff} and σ^{eff}) are usually reduced within a porous electrode relative to their bulk values. Generally, the effect of volume fraction and tortuosity of the phase of interest on property ψ is accounted for by Bruggeman's relation, $\psi^{eff} = \psi_\infty \varepsilon^\beta$, where β is Bruggeman's exponent. The diffusional conductivity is given by [22]

$$\kappa_D^{eff} = \frac{2RT\kappa^{eff}}{F}(t_+^0 - 1)\left(1 + \frac{d\ln f_\pm}{d\ln c_e}\right) \tag{7}$$

where $f_\pm$ is mean molar activity coefficient of the electrolyte.

Now, in the presence of an SEI layer at the negative electrode, the Butler-Volmer intercalation current density there is driven by a slightly modified overpotential, i.e.,

$$\eta_n = \phi_s - \phi_e - U_n - R_f F(j_i + j_s) \tag{8}$$

with R_f denoting the SEI film resistance. We assume that the side reaction kinetics can be modeled in terms of a Tafel expression, i.e.,

$$j_s = -\frac{i_{0s}}{F}\exp\left(-\frac{F\eta_s}{2RT}\right) \tag{9}$$

where the side reaction overpotential is given by

$$\eta_s = \phi_s - \phi_e - U_s^{ref} - R_f F(j_i + j_s) \tag{10}$$

Based on Eqs. (8) and (10) we see that for calculating both the side reaction and intercalation current densities the following nonlinear system

$$j_i = 2\frac{i_0}{F}\sinh\left[\frac{F}{2RT}(\phi_s - \phi_e - U_n) - \frac{F^2}{2RT}R_f(j_i + j_s)\right] \tag{11}$$

$$j_s = -\frac{i_{0s}}{F}\exp\left[-\frac{F}{2RT}(\phi_s - \phi_e - U_s^{ref}) + \frac{F^2}{2RT}R_f(j_i + j_s)\right] \tag{12}$$

has to be solved at each location in the negative electrode, at each time step during the integration of the species, charge, and energy balance (further addressed below) equations, while in the charge portion of a charge/discharge cycle. (Similarly, during the discharge portion, the deintercalation current density at each

location in the negative electrode has to be determined by solving a nonlinear equation.) Having determined the side reaction current density, the temporal evolution of the SEI film thickness follows from Faraday's law:

$$\frac{\partial \delta_f}{\partial t} = -\frac{j_s}{\rho_{\text{SEI}}/M_{\text{SEI}}} \tag{13}$$

where $\rho_{\text{SEI}}/M_{\text{SEI}}$ is the molar density of the product material in the SEI film. This allows the SEI film resistance to be calculated as

$$R_f = R_{\text{SEI}} + \frac{\delta_f}{\kappa_{\text{SEI}}} \tag{14}$$

where κ_{SEI} is the SEI film conductivity, while R_{SEI} is the SEI layer resistance at the initial time (corresponding to a zero film thickness), which has to be regarded as a known quantity. Finally, in addition to the impedance rise noted above, there is a capacity loss caused by the side reaction current during charging, which can be obtained from the relation

$$\dot{q}_{lost} = -FAa_{s,n}\int_0^{\delta_n} j_s \, dx \tag{15}$$

with δ_n and A denoting the negative electrode thickness and (transversal) surface area.

Although the P2D model developed thus far accounts for dissipative phenomena within a cell and is able to predict isothermal electrochemical performance (such as, e.g., voltage response, potential and concentration profiles based on a constant or time-varying current density input), strictly speaking it cannot be used for investigating aging phenomena since it neglects the thermal/electrochemical coupling that arises as a consequence of the temperature depedence of the cell physico-chemical properties (such as, e.g., lithium-ion diffusivities and conductivities and any additional side reaction rates) and the heat generation term in the energy balance equation. (As is well known, the thermal behavior of a lithium-ion cell has a dramatic impact on its cycle life and, in particular, on the initiation of degradation processes [30, 54].) Therefore, to date the P2D (as well as more complex multiscale derivative models) has been addressed in a number of studies focused on its coupling to a thermal model [55, 56, 57, 46, 58, 59, 60, 61]. Herein, given our focus on the thermal behavior of a single cell, we are going to rely on a simplified (macroscale) energy balance

equation in 1D, that assumes a binary electrolyte and neglects phase change effects as well as the enthalpy of mixing of all relevant phases [55, 56]:

$$\frac{\partial}{\partial t}(\rho c_{_P} T) = \frac{\partial}{\partial x}\left(\lambda \frac{\partial T}{\partial x}\right) + \dot{q} \tag{16}$$

with the heat generation rate given by

$$\begin{aligned}\dot{q} = a_s F(j_i + j_s)\left[\eta - R_f F(j_i + j_s)\right] + a_s F(j_i + j_s) T \frac{\partial U}{\partial T} \\ + \sigma^{\mathit{eff}} \left(\frac{\partial \phi_s}{\partial x}\right)^2 + \kappa^{\mathit{eff}} \left(\frac{\partial \phi_e}{\partial x}\right)^2 + \kappa_D^{\mathit{eff}} \frac{\partial \phi_e}{\partial x} \frac{\partial \ln c_e}{\partial x}\end{aligned} \tag{17}$$

The first term on the RHS is the irreversible heat due to the deviation of the cell operating potential from its equilibrium potential (a.k.a. active polarization heat [62]) and can be traced to a charge transfer resistance at the solid/electrolyte interface that hinders the intercalation (or deintercalation) process. The second term represents a reversible heat since it originates in the entropy change associated with electrochemical reactions. (Consequently, it is also known as reaction or entropic heat.) Finally, the last three terms can be traced to the ohmic (or Joule) heating due to a transport resistance in the solid and electrolyte phases. Boundary conditions for the energy equation above have to be imposed at the current collectors and involve a (convective) heat transfer coefficient h, i.e.,

$$-\lambda \left.\frac{\partial T}{\partial x}\right|_{x=0} = h\left[T_{ref} - T(0,t)\right], \quad \text{and} \quad -\lambda \left.\frac{\partial T}{\partial x}\right|_{x=L} = h\left[T(L,t) - T_{ref}\right] \tag{18}$$

with $T_{ref} = 298.15\,\mathrm{K}$ denoting the surrounding ambient temperature. Note that since the temperature dependence for many quantities in the cell model introduced thus far is unknown, that is usually modeled in terms of an empirical Arrhenius relationship, relating some property of the cell at temperature T, $\psi(T)$, to the same property evaluated at reference temperature T_{ref}, ψ_{ref}, via an exponential function having activation energy E_a, i.e.,

$$\psi(T) = \psi_{ref} \exp\left\{-\frac{E_a}{R}\left(\frac{1}{T} - \frac{1}{T_{ref}}\right)\right\} \tag{19}$$

In particular, Arrhenius factors are employed in the cell model for the solid phase diffusivities in both electrodes, as well as for the reaction rate constants in the Butler-Volmer exchange current density.

The liquid electrolyte considered herein is 1 M $LiPF_6$ dissolved into a mixture

of ethylene carbonate (EC) and dimethyl carbonate (DMC) with a 2:1 volume ratio. In fact, a number of experimental studies have shown that the transport properties of $LiPF_6$ in carbonate solvents are strong functions of c_e and T but a much weaker function of the formulation of the carbonate mixture. Following Valøen and Reimers [63], we elect to model the Li^+ diffusivity in the electrolyte using the expression

$$\log_{10} D_e = \frac{1}{\ln 10}\left[-4.43 - \frac{54}{T - 229 - 5c_e} - 0.22c_e\right] \tag{20}$$

(D_e in this expression is in cm^2/s, c_e in mol/dm^3, while T is in K). Similarly, based on another fit to experimental measurements, the following model expression is employed for the electrolyte conductivity [63]:

$$\sqrt{\frac{\kappa_e}{c_e}} = -10.5 + 0.074\,T - 6.96\,10^{-5}\,T^2 + 0.668\,c_e - 0.0178\,c_eT + 2.8\,10^{-5}\,c_eT^2 + 0.494\,c_e^2 - 8.86\,10^{-4}\,c_e^2T \tag{21}$$

(κ_e in this expression is in mS/cm, c_e in mol/dm^3, while T is in K). Note that all results presented below were computed by neglecting the mean molar activity coefficient of the salt in an EC/DMC mixture, equivalent to assuming a unit value for the thermodynamic factor $\left(1 + \frac{d\ln f_\pm}{d\ln c_e}\right)$.

3. Numerical methods

The starting point for the numerical work described herein was the observation that although a Fortran code (known as Dualfoil) for the original P2D model (i.e., ignoring aging effects) had been developed and validated (and made available in the public domain) by Doyle et al. [21, 22, 47, 48, 49], subsequently a number of numerical implementations of the P2D model have been proposed in the literature that mainly address its computational complexity in terms of (i) additional simplifying assumptions (i.e., model order reduction), and (ii) more (or less) efficient numerical methods. Particularly in the latter category, it should be acknowledged that a number of methods have been employed to discretize the spatial coordinates in the P2D model, including finite differences [21, 39], Galerkin-based collocation [64], orthogonal collocation on finite elements [65], and orthogonal collocation with coordinate transformation [66], to

name a few. In fact, computationally efficient discretizations of the P2D model based on finite volumes have also been reported [67, 68]. In the initial stages of this work, we ultimately chose the finite-volume code by Torchio et al. [68] (a.k.a. LIONSIMBA) since, in addition to the well-known advantages afforded by a finite-volume scheme over comparable finite-difference or finite-element spatial discretizations, a detailed procedure for the numerical implementation of the original P2D model into a Matlab code that leverages the SUNDIALS suite of temporal integrators [69] has been thoroughly documented in their paper [68].

In conclusion, Eqs. (11)–(12) and (15) summarize the details of our numerical setup. In the extended LIONSIMBA code considered herein, we noticed that a fixed-point iteration did not always work for solving Eqs. (11)–(12), so in our production runs we chose to rely on Newton's method. In addition, as to the inclusion of an additional ODE [Eq. (15)] in the system of equations passed to IDA [69], we first coded the equation $\dot{q}_{lost} = const$ (equal to 1 during the charge portion of a cycle and zero otherwise) as a verification test and checked that the temporal history for q_{lost} from such a test was a staircase in time (the non-constant portions being ramp-like). The remaining details are the same as discussed by Torchio et al. [68].

4. Influence of aging model parameters on charge/discharge performance

We investigate the same lithium-ion cell (based on a $LiCoO_2|LiC_6$ couple) as in Cai and White [46], for which parameter values are presented in Tables 1 and 2. Such parameter values are in fact representative of actual lithium-ion cells, since they had been obtained via an estimation procedure by systematically comparing simulated discharge profiles with experimental discharge data for lithium-ion pouch cells [57].

Before actually running P2D simulations of an aging cell under cyclic loading conditions, we ran a test case consisting in an isothermal galvanostatic discharge simulation with the cell operated at different C rates. [Near-isothermal conditions were obtained by imposing a value $h = 1000\,\mathrm{W/(m^2\,K)}$ for the (convective) heat transfer coefficient at each current collector boundary.] Numerical results from the test case just mentioned (see Fig. 1) show discharge times that can be

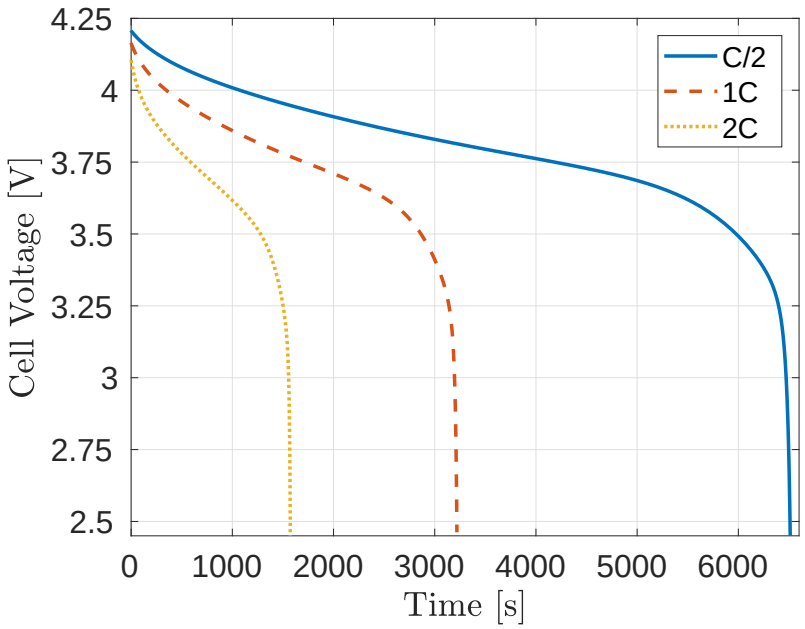

Figure 1: Cell voltage vs. time from isothermal discharge simulations of the Cai and White [46] cell operated at different C rates.

checked *a posteriori* based on the approximate relation

$$\frac{q}{A} \approx F\delta\varepsilon_s c_{s,max}(\theta_0 - \theta_f) \tag{22}$$

with q denoting capacity. All quantities on the RHS refer to the negative electrode; in particular, θ_0 and θ_f denote the initial and final values for the negative electrode state of charge (SOC), defined as

$$\theta(t) = \frac{1}{\delta_n}\int_0^{\delta_n} \frac{\bar{c}_s(x,t)}{c_{s,max}}\,dx \tag{23}$$

with $\bar{c}_s$ indicating a spherically-averaged solid phase concentration. Equation (22) has been discussed in the literature many times [70, 71, 72] since it readily follows as a consequence of the (isothermal) P2D equations (ignoring aging effects); it is useful for connecting electrode capacity to its state of charge. In fact, since in a galvanostatic discharge the LHS of Eq. (22) can also be evaluated as $\frac{I_a}{A}t$, we see that with the parameter values in Table 2 we obtain

$$t_{dis} \approx \frac{F\delta\varepsilon_s c_{s,max}(\theta_0 - \theta_f)}{I_a/A} = 6467,\, 3178,\, 1527.8\,s \tag{24}$$

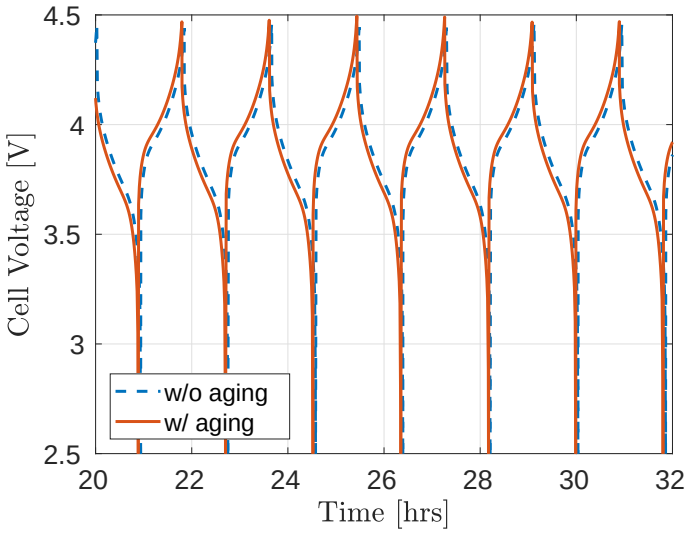

(a)

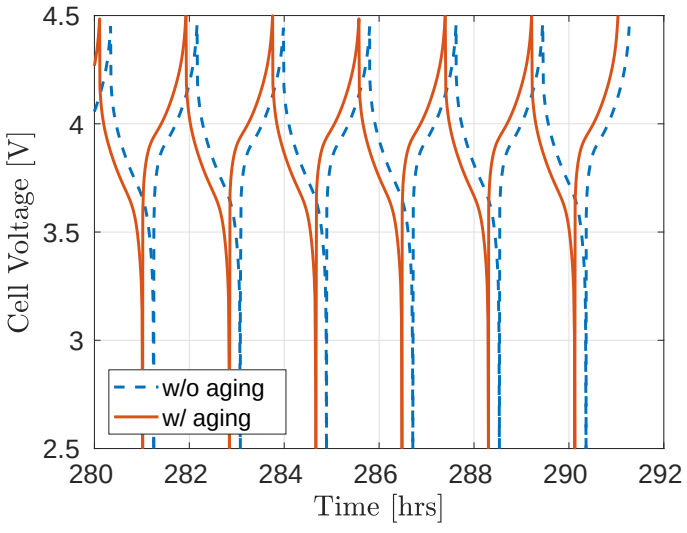

(b)

Figure 2: Cell voltage vs. time with and without aging effect. (a) Initially, the voltage profiles from the aged and ideal cells are essentially coincident. After 20 hours of operation, we see only a slight discrepancy between the two cases. (b) Voltage profiles after 280 hours of operation (last 6 of 160 cycles are shown).

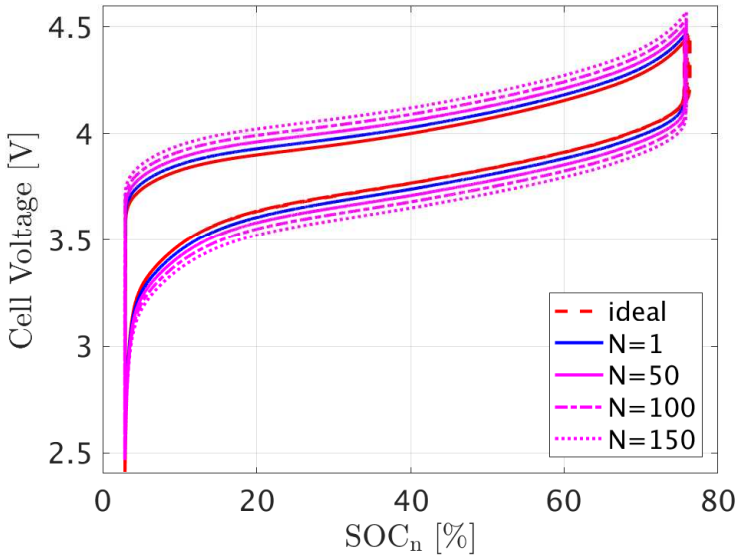

Figure 3: Cell voltage vs. negative electrode SOC for cyclic operation of an aging cell vs. that for an "ideal" (i.e., ignoring aging effects) cell. N is for cycle number in the case with aging.

in the C/2, 1C, and 2C cases, respectively, in good agreement with Fig. 1; in fact, we see that the associated relative errors (which turn out to be 0.67 %, 1.2 %, and 2.8 % in each of the aforementioned cases) increase as the C rate increases, due to the presumption [built into Eq. (22)] that lithium concentration at the surface of an active particle is equal to its average concentration and uniform throughout the electrode. In terms of accuracy, that is a reasonable assumption for low charge/discharge current densities (as discussed at length by Rahn and Wang [72]).

We now show the results of numerical simulations of Newman's thermal-electrochemical P2D model augmented with the simple aging model above to elucidate the influence of aging model parameters on cell performance after a relatively small number (160) of galvanostatic charge-discharge cycles. Figure 2 shows temporal histories for cell voltage (with both the charge and discharge portions of a cycle operated at 1C) for an aging cell vs. that for an "ideal" (i.e., with no aging) cell, in both cases with a large value for the heat exchange coefficient [i.e., $h = 100\,\mathrm{W/(m^2\,K)}$], so as to be able to reproduce near-isothermal conditions. As can be seen, during the first few hours of operation, the temporal

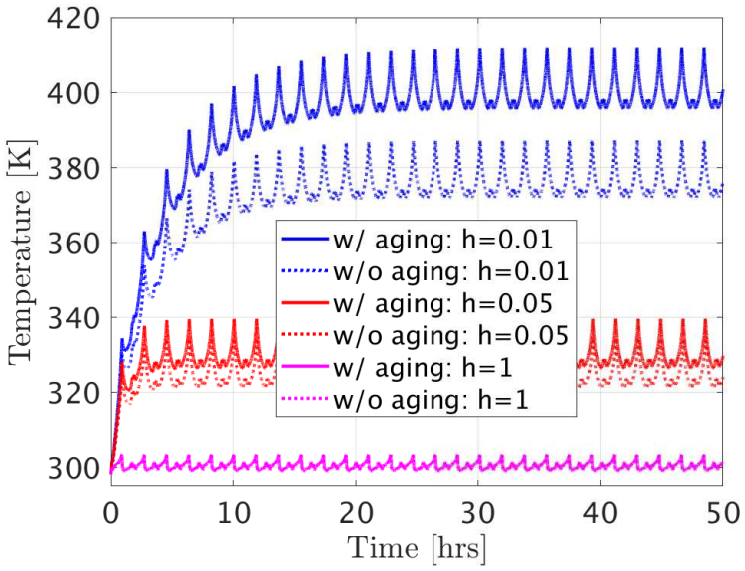

Figure 4: Surface cell temperature vs. time for an aging cell (solid) vs. that for an "ideal" (i.e., ignoring aging effect) cell (dotted) with different values of heat exchange coefficient. [N.B. h values shown in the legend are in $\mathrm{W/(m^2\,K)}$.]

histories are almost coincident, since the internal resistance of the cell is almost the same as the initial SEI layer resistance (taken to be $R_{\mathrm{SEI}} = 10^{-2}\,\Omega\,\mathrm{m}^2$). Later on, the SEI layer starts to grow over the charge portions of the subsequent cycles, and finally its effect becomes significant, as evinced after 154 cycles of operation. In fact, when those histories are replotted vs. the negative electrode SOC, we see that for an "ideal" cell the energy dissipated during each cycle stays constant in time, while for an aging cell it keeps increasing with cycle number (see Fig. 3).

We briefly investigate the influence of the aging model as it affects surface cell temperature for different values of the (convective) heat transfer coefficient h. Based on the temporal histories for surface cell temperature in Fig. 4, the aging model has virtually no effect on the surface cell temperature in terms of deviations from the "ideal" case for values of h larger than about $1\,\mathrm{W/(m^2\,K)}$; in particular, for that value of h the surface cell temperature can be described as consisting of small amplitude (deterministic) fluctuations superimposed on a constant mean value (equal to the surrounding ambient temperature $T_{ref} = 298.15\,\mathrm{K}$). For smaller h values, however, an aging cell has a higher surface

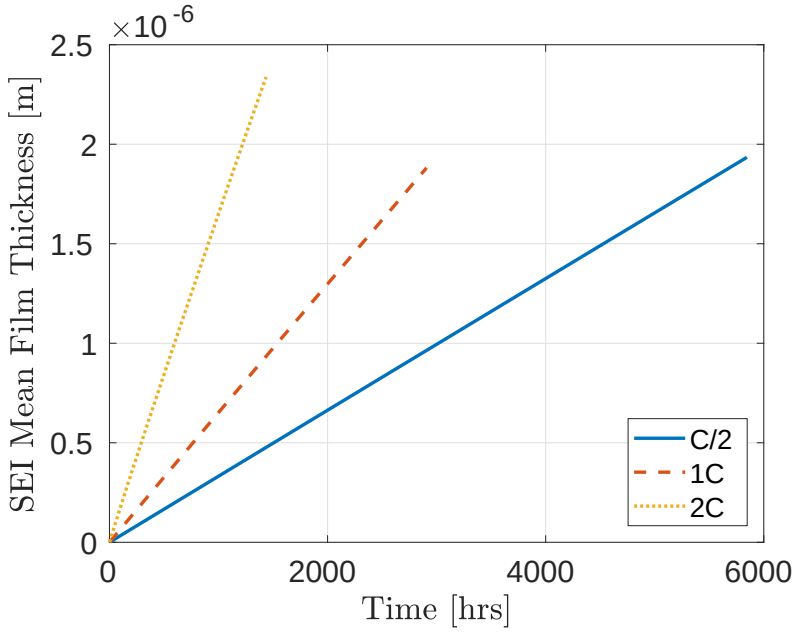

Figure 5: Temporal histories for SEI mean film thickness for an aging cell after 1600 cycles of operation at different C rates.

temperature than in the "ideal" case, and, simultaneously, larger amplitude (deterministic) fluctuations appear to be superimposed on a longer transient (as h decreases) before a steady state is reached.

We now discuss the influence of an applied current density other than 1C, as it affects both capacity fade and the rate of SEI layer growth. Particularly with respect to the latter, increasing the applied C rate leads (as expected) to accelerated SEI layer growth since a larger current density leads to an increase in side reaction overpotential and current density, which translates into a larger growth rate for the SEI film thickness (see Fig. 5). As can be seen, even though the range of simulated times corresponds now to over 1000 cycles, we only see a linear regime of SEI layer growth (with a growth rate of about 0.64 nm/hr at 1C), with no indications of "saturation" (i.e., sublinear growth) in the growth law as the cycle number grows unbounded. This is not satisfactory when it comes to comparing simulations to experimental data; however, it should be acknowledged that the aging model employed herein can only reproduce a linear growth regime since it does not account for any diffusive transport limitations during new SEI formation. In fact, assuming that the rate-limiting step during new SEI

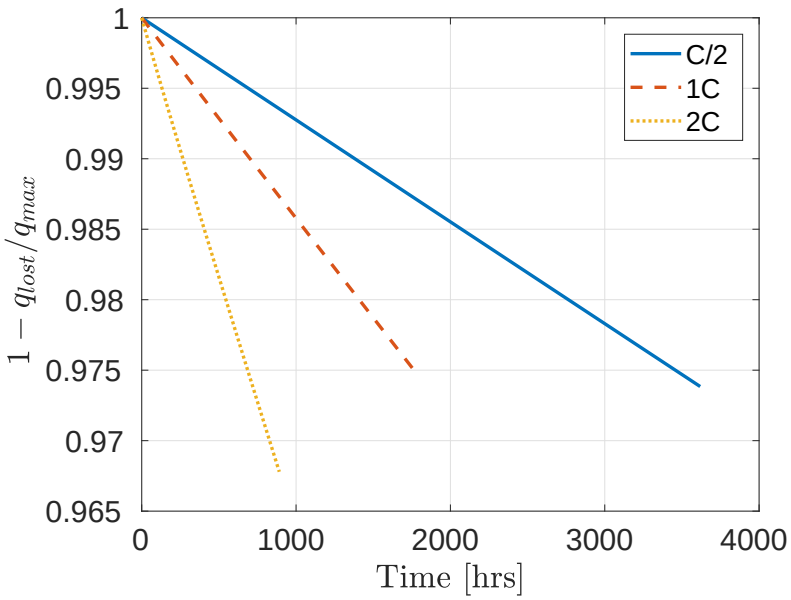

Figure 6: Normalized cell capacity vs. time for cyclic operation of an aging cell at different C rates.

formation corresponds to the reduction of ethylene-carbonate molecules to yield an anion radical, and including an additional advection-diffusion equation in the aging model to obtain an improved estimate of the side reaction rate, Safari and Delacourt [73] were able to show good agreement between model predictions and experimental data for the temporal evolution of the SEI film thickness from a set of $LiFePO_4$/graphite cells. Extensive simulations of SEI layer growth under mixed control (i.e., ethylene carbonate diffusion across the SEI film and side reaction kinetics) within an electrochemical-thermal P2D model have also been demonstrated by Liu et al. [31]. Finally, it is worth noting that Xie et al. [74] have proposed a similar electrochemical-thermal P2D aging model, but assuming that the SEI film thickness follows the purely diffusive growth law obtained by Ploehn et al. [18] (i.e., disregarding Faraday's law for computing the temporal evolution of the SEI film thickness). Clearly, this seems to be an inexpensive fix to the purely kinetics-driven aging model to enable a comparison of model predictions with experimental data for SEI film thickness; however, we leave this matter for future work to be presented in a subsequent publication, that will include a comparison between simulation data and experimental results.

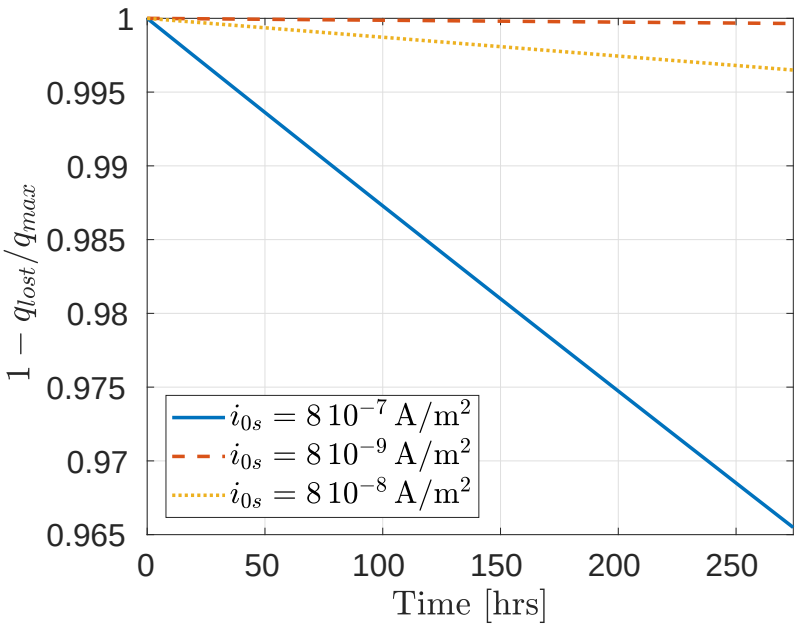

Figure 7: Normalized cell capacity vs. time for cyclic operation of an aging cell for different values of side reaction exchange current density.

Returning to our model predictions depending on the applied C rate, we show once more (Fig. 6) that a larger applied current density during multiple galvanostatic charge/discharge cycles also corresponds to a faster capacity loss (as compared to a smaller C rate), as can be seen from the temporal evolution of the normalized cell capacity, defined as $1 - \frac{q_{lost}}{q_{max}}$, where the initial (maximum) charge was estimated using Eq. (22).

Note that since herein the side reaction exchange current density is an adjustable parameter, it is important to explore different values of i_{0s} for accurate capacity fade modeling. As expected, larger values of i_{0s} lead to an accelerated side reaction, which translates into a strictly monotonic dependence of the temporal evolution of the normalized cell capacity as a function of i_{0s} (see Fig. 7). In fact, a similar strictly monotonic dependence of capacity fade on i_{0s} could be hypothesized based on Fig. 8, showing cell voltage profiles after 159 cycles of operation as a function of the side reaction exchange current density.

Finally, we briefly comment on our capacity fade results depending on an (assumed) value of SEI film conductivity. As can be seen (Fig. 9), cell voltage profiles as a function of (a reciprocal) SEI film conductivity show a similar

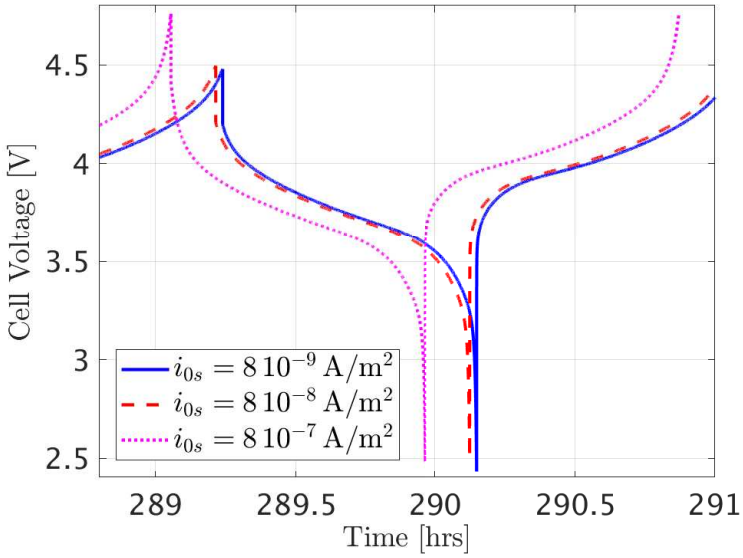

Figure 8: Cell voltage profiles for the last cycle (in a series of 160) for an aging cell with different values of side reaction exchange current density.

aging behavior (i.e., for decreasing values of SEI film conductivity) to that exhibited when (other parameters the same) we consider increasing values of the side reaction exchange current density (Fig. 8). [Incidentally, note that very similar plots showing voltage profiles after a relatively large number of charge/discharge cycles as a function of i_{0s} and κ_{SEI} have also been presented by Ashwin et al. [75], who reported capacity fade simulations of the Ramadass et al. [4] model (built on top of an electrochemical-thermal P2D model) in application to a $LiCoO_2$/graphite cell, with the model further improved by means of an evolution equation for the liquid electrolyte volume fraction as a function of its partial molar volume, thereby providing a stronger coupling between cell performance and chemical properties of the electrolyte.] Consequently, based on the plots in Fig. 9 we should expect a faster capacity fade for decreasing values of SEI film conductivity. However, plots of temporal evolution for the normalized cell capacity as a function of SEI film conductivity (Fig. 10) show that decreasing values of κ_{SEI} actually translate into a slower capacity fade. In fact, there is only a weak indication of such a monotonic dependence in Fig. 10, even when the range of simulated times corresponds to over 1000 cycles.

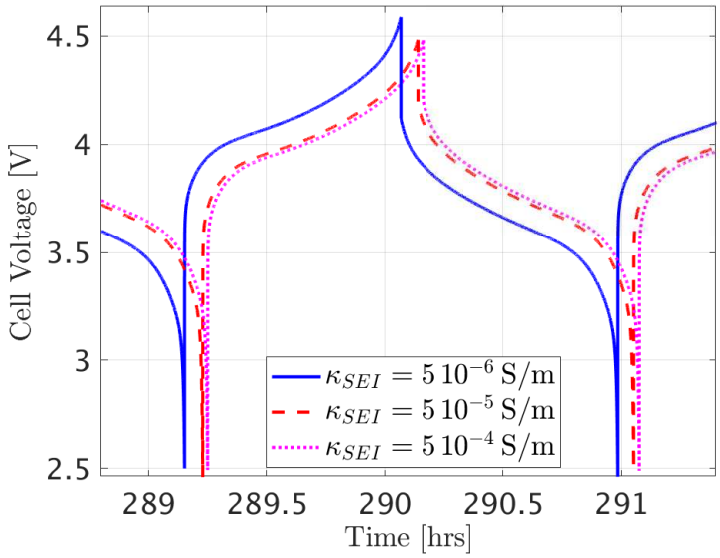

Figure 9: Cell voltage profiles for the last cycle (in a series of 160) for an aging cell with different values of SEI layer conductivity.

In conclusion, for accurate capacity fade modeling it is critical to provide estimates of i_{0s} and κ_{SEI}, which mainly depends on the choice of electrolyte formulation.

5. Conclusions

We have discussed preliminary results from simulations of the Ramadass et al. [4] model of aging built on top of an electrochemical-thermal (P2D) coupled model of "ideal" (i.e., ignoring aging phenomena) cell dynamics by means of a finite-volume Matlab code. Capacity fade has been assessed by integrating in time the equation for the loss of cyclable lithium ions that arises as a result of a single irreversible electrolyte decomposition reaction in the aging model. In particular, we have shown that assuming cyclic operation of an "ideal" cell, its energy dissipation (per cycle) is constant as a function of cycle number, while that same quantity keeps increasing with cycle number for an aging cell. Also, the surface cell temperature vs. time dependences for large values of a (convective) heat transfer coefficient show a negligible effect of the aging model in terms of deviations from the corresponding temporal histories for an "ideal"

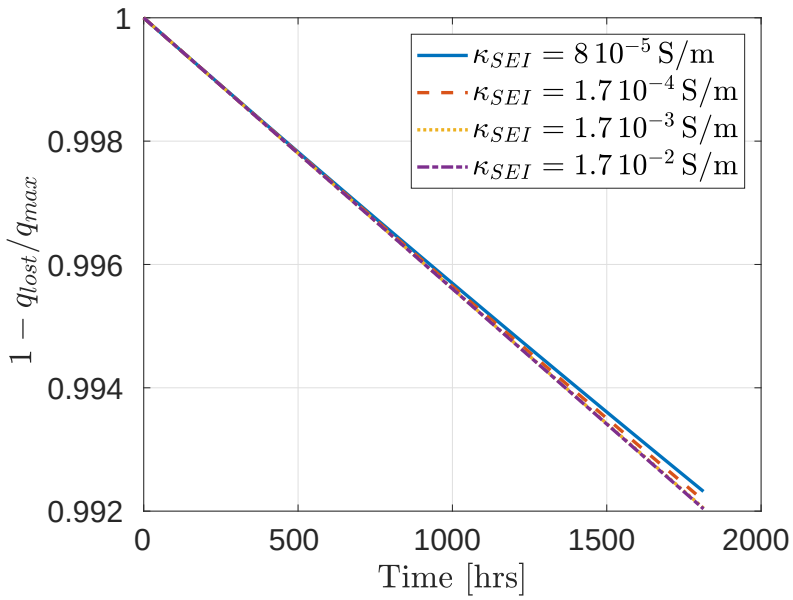

Figure 10: Normalized cell capacity vs. time after 1600 cycles of operation for an aging cell for different values of SEI film conductivity.

cell; however, for decreasing values of the heat transfer coefficient the surface cell temperature for an aging cell turns out to be systematically larger than that for an "ideal" cell.

Acknowledgements

This work was supported by the PROT-ONE Project, FAR-FAS 2014, CUP 4421.02102014.07200099, funded by Regione Toscana.

References

[1] R. Darling, J. Newman, Modeling side reactions in composite $Li_yMn_2O_4$ electrodes, J. Electrochem. Soc. 145 (3) (1998) 990–8.

[2] P. Arora, M. Doyle, R. E. White, Mathematical modeling of the lithium deposition overcharge reaction in lithium-ion batteries using carbon-based negative electrodes, J. Electrochem. Soc. 146 (10) (1999) 3543–53.

[3] J. Christensen, J. Newman, A mathematical model for the lithium-ion negative electrode solid electrolyte interphase, J. Electrochem. Soc. 151 (11) (2004) A1977–88.

[4] P. Ramadass, B. Haran, P. M. Gomadam, R. White, B. Popov, Development of first-principles capacity fade model for Li-ion cells, J. Electrochem. Soc. 151 (2) (2004) A196–203.

[5] M. Safari, M. Morcrette, A. Teyssot, C. Delacourt, Multimodal physics-based aging model for life prediction of Li-ion batteries, J. Electrochem. Soc. 156 (3) (2009) A145–53.

[6] D. Aurbach, Y. Talyosef, B. Markovsky, E. Markevich, E. Zinigrad, L. Asraf, J. S. Gnanaraj, H.-J. Kim, Design of electrolyte solutions for Li and Li-ion batteries: A review, Electrochim. Acta 50 (2-3) (2004) 247–54.

[7] Q. Zhang, R. E. White, Capacity fade analysis of a lithium ion cell, J. Power Sources 179 (2) (2008) 793–8.

[8] D. P. Abraham, E. M. Reynolds, E. Sammann, A. N. Jansen, D. W. Dees, Aging characteristics of high-power lithium-ion cells with $LiNi_{0.8}Co_{0.15}Al_{0.05}O_2$ and $Li_{4/3}Ti_{5/3}O_4$ electrodes, Electrochim. Acta 51 (3) (2005) 502–10.

[9] P. Lu, C. Li, E. W. Schneider, S. J. Harris, Chemistry, impedance, and morphology evolution in solid electrolyte interphase films during formation in lithium ion batteries, J. Phys. Chem. C 118 (2) (2014) 896–903.

[10] J. Li, E. Murphy, J. Winnick, P. Kohl, Studies on the cycle life of commercial lithium ion batteries during rapid charge–discharge cycling, J. Power Sources 102 (1-2) (2001) 294–301.

[11] X. Han, M. Ouyang, L. Lu, J. Li, Y. Zheng, Z. Li, A comparative study of commercial lithium ion battery cycle life in electrical vehicle: Aging mechanism identification, J. Power Sources 251 (2014) 38–54.

[12] D. Aurbach, B. Markovsky, A. Shechter, Y. Ein-Eli, H. Cohen, A comparative study of synthetic graphite and Li electrodes in electrolyte solutions based on ethylene carbonate-dimethyl carbonate mixtures, J. Electrochem. Soc. 143 (12) (1996) 3809–20.

[13] J. Vetter, P. Novak, M. R. Wagner, C. Veit, K.-C. Möller, J. O. Basenhard, M. Winter, M. Wolfahrt-Mehrens, C. Vogler, A. Hammouche, Ageing mechanisms in lithium-ion batteries, J. Power Sources 147 (1-2) (2005) 269–81.

[14] D. Aurbach, B. Markovsky, I. Weissman, E. Levi, Y. Ein-Eli, On the correlation between surface chemistry and performance of graphite negative electrodes for Li ion batteries, Electrochim. Acta 45 (1-2) (1999) 67–86.

[15] A. V. Churikov, Transfer mechanism in solid-electrolyte layers on lithium: Influence of temperature and polarization, Electrochim. Acta 46 (15) (2001) 2415–26.

[16] I. Nainville, A. Lemarchand, J.-P. Badiali, Passivation of a lithium anode: A simulation model, Electrochim. Acta 41 (18) (1996) 2855–63.

[17] O. Pensado-Rodriguez, J. R. Flores, M. Urquidi-Macdonald, D. D. Macdonald, Electrochemical behavior of lithium in alkaline aqueous electrolytes. II. Point defect model, J. Electrochem. Soc. 146 (4) (1999) 1326–35.

[18] H. J. Ploehn, P. Ramadass, R. E. White, Solvent diffusion model for aging of lithium-ion battery cells, J. Electrochem. Soc. 151 (3) (2004) A456–62.

[19] Y.-G. Ryu, S.-l. Pyun, Passivation kinetics of surface films formed on a graphite electrode in organic lithium salt solution as a function of salt anion type, J. Electroanal. Chem. 433 (1-2) (1997) 97–105.

[20] D. Aurbach, Review of selected electrode–solution interactions which determine the performance of Li and Li ion batteries, J. Power Sources 89 (2) (2000) 206–18.

[21] M. Doyle, T. F. Fuller, J. Newman, Modeling of galvanostatic charge and discharge of the lithium/polymer/insertion cell, J. Electrochem. Soc. 140 (6) (1993) 1526–33.

[22] T. F. Fuller, M. Doyle, J. Newman, Simulation and optimization of the dual lithium ion insertion cell, J. Electrochem. Soc. 141 (1) (1994) 1–10.

[23] J. Newman, D. Bennion, C. W. Tobias, Mass transfer in concentrated binary electrolytes, Ber. Bunsenges. Physik. Chem. 69 (7) (1965) 608–12, Corrections: *ibid.* 70 (4) (1966) 493.

[24] J. Newman, Transport processes in electrolytic solutions, in: C. W. Tobias (Ed.), Advances in Electrochemistry and Electrochemical Engineering, Vol. 5, Wiley Interscience Publishers, 1967, pp. 87–135.

[25] J. Newman, T. W. Chapman, Restricted diffusion in binary solutions, AIChE J. 19 (2) (1973) 343–48.

[26] J. Newman, K. E. Thomas-Alyea, Electrochemical Systems, 3rd Edition, Wiley, Hoboken, NJ, 2004.

[27] J. S. Newman, C. W. Tobias, Theoretical analysis of current distribution in porous electrodes, J. Electrochem. Soc. 109 (12) (1962) 1183–91.

[28] A. M. Johnson, J. Newman, Desalting by means of porous carbon electrodes, J. Electrochem. Soc. 118 (3) (1971) 510–7.

[29] J. Newman, W. Tiedemann, Porous-electrode theory with battery applications, AIChE J. 21 (1) (1975) 25–41.

[30] T. M. Bandhauer, S. Garimella, T. F. Fuller, A critical review of thermal issues in lithium-ion batteries, J. Electrochem. Soc. 158 (3) (2011) R1–25.

[31] L. Liu, J. Park, X. K. Lin, A. M. Sastry, W. Lu, A thermal-electrochemical model that gives spatial-dependent growth of solid electrolyte interphase in a Li-ion battery, J. Power Sources 268 (2014) 482–90.

[32] R. E. Gerver, J. P. Meyers, Three-dimensional modeling of electrochemical performance and heat generation of lithium-ion batteries in tabbed planar configurations, J. Electrochem. Soc. 158 (7) (2011) A835–43.

[33] J. Christensen, D. Cook, P. Albertus, An efficient parallelizable 3D thermo-electrochemical model of a Li-ion cell, J. Electrochem. Soc. 160 (11) (2013) A2258–67.

[34] A. Awarke, S. Pischinger, J. Ogrzewalla, Pseudo 3D modeling and analysis of the SEI growth distribution in large format Li-ion polymer pouch cells, J. Electrochem. Soc. 160 (1) (2013) A172–81.

[35] S. U. Kim, P. Albertus, D. Cook, C. W. Monroe, J. Christensen, Thermo-electrochemical simulations of performance and abuse in 50-Ah automotive cells, J. Power Sources 268 (2014) 625–33.

[36] R. Zhao, J. Liu, J. Gu, The effects of electrode thickness on the electrochemical and thermal characteristics of lithium ion battery, Appl. Energy 139 (2015) 220–9.

[37] S. Panchal, I. Dincer, M. Agelin-Chaab, R. Fraser, M. Fowler, Transient electrochemical heat transfer modeling and experimental validation of a large sized $LiFePO_4$/graphite battery, Int. J. Heat Mass Transf. 109 (2017) 1239–1251.

[38] S. Panchal, M. Mathew, R. Fraser, M. Fowler, Electrochemical thermal modeling and experimental measurements of 18650 cylindrical lithium-ion battery during discharge cycle for an EV, Appl. Therm. Eng. 135 (2018) 123–32.

[39] G. G. Botte, V. R. Subramanian, R. E. White, Mathematical modeling of secondary lithium batteries, Electrochim. Acta 45 (15-16) (2000) 2595–609.

[40] P. M. Gomadam, J. W. Weidner, R. A. Dougal, R. E. White, Mathematical modeling of lithium-ion and nickel battery systems, J. Power Sources 110 (2) (2002) 267–84.

[41] K. E. Thomas, J. Newman, R. M. Darling, Mathematical modeling of lithium batteries, in: W. A. V. Schalkwijk, B. Scrosati (Eds.), Advances in Lithium-Ion Batteries, Springer, 2002, pp. 345–92.

[42] J. Newman, K. E. Thomas, H. Hafezi, D. R. Wheeler, Modeling of lithium-ion batteries, J. Power Sources 119 (2003) 838–43.

[43] S. Santhanagopalan, Q. Guo, P. Ramadass, R. E. White, Review of models for predicting the cycling performance of lithium ion batteries, J. Power Sources 156 (2) (2006) 620–8.

[44] A. Jokar, B. Rajabloo, M. Désilets, M. Lacroix, Review of simplified pseudo-two-dimensional models of lithium-ion batteries, J. Power Sources 327 (2016) 44–55.

[45] A. Lamorgese, R. Mauri, B. Tellini, Derivation of governing equation system for electrochemical-thermal P2D aging model of a $LiCoO_2$/graphite cell, Data Brief (submitted).

[46] L. Cai, R. E. White, Mathematical modeling of a lithium-ion battery with thermal effects in COMSOL Inc. Multiphysics (MP) software, J. Power Sources 196 (2011) 5985–89.

[47] M. Doyle, T. F. Fuller, J. Newman, The importance of the lithium ion transference number in lithium/polymer cells, Electrochim. Acta 39 (13) (1994) 2073–81.

[48] M. Doyle, J. Newman, The use of mathematical modeling in the design of lithium/polymer battery systems, Electrochim. Acta 40 (13-14) (1995) 2191–6.

[49] C. M. Doyle, Design and simulation of lithium rechargeable batteries, Ph.D. thesis, University of California, Berkeley (1995).

[50] O. Y. Egorkina, A. M. Skundin, The effect of temperature on lithium intercalation into carbon materials, J. Solid State Electrochem. 2 (4) (1998) 216–20.

[51] K. E. Thomas, J. Newman, Heats of mixing and of entropy in porous insertion electrodes, J. Power Sources 119 (2003) 844–9.

[52] V. V. Viswanathan, D. Choi, D. Wang, W. Xu, S. Towne, R. E. Williford, J.-G. Zhang, J. Liu, Z. Yang, Effect of entropy change of lithium intercalation in cathodes and anodes on Li-ion battery thermal management, J. Power Sources 195 (11) (2010) 3720–9.

[53] M. Guo, G. Sikha, R. E. White, Single-particle model for a lithium-ion cell: Thermal behavior, J. Electrochem. Soc. 158 (2) (2011) A122–32.

[54] C.-F. Chen, P. Barai, P. P. Mukherjee, An overview of degradation phenomena modeling in lithium-ion battery electrodes, Curr. Opin. Chem. Eng. 13 (2016) 82–90.

[55] W. B. Gu, C. Y. Wang, Thermal-electrochemical modeling of battery systems, J. Electrochem. Soc. 147 (8) (2000) 2910–22.

[56] C. Y. Wang, V. Srinivasan, Computational battery dynamics (CBD)–electrochemical/thermal coupled modeling and multi-scale modeling, J. Power Sources 110 (2) (2002) 364–76.

[57] K. Kumaresan, G. Sikha, R. E. White, Thermal model for a Li-ion cell, J. Electrochem. Soc. 155 (2) (2008) A164–71.

[58] G.-H. Kim, K. Smith, K.-J. Lee, S. Santhanagopalan, A. Pesaran, Multi-domain modeling of lithium-ion batteries encompassing multi-physics in varied length scales, J. Electrochem. Soc. 158 (8) (2011) A955–69.

[59] M. Guo, G.-H. Kim, R. E. White, A three-dimensional multi-physics model for a Li-ion battery, J. Power Sources 240 (2013) 80–94.

[60] K.-J. Lee, K. Smith, A. Pesaran, G.-H. Kim, Three dimensional thermal-, electrical-, and electrochemical-coupled model for cylindrical wound large format lithium-ion batteries, J. Power Sources 241 (2013) 20–32.

[61] A. Latz, J. Zausch, Thermal-electrochemical lithium-ion battery simulations on microstructure and porous electrode scale, ECS Trans. 69 (1) (2015) 75–81.

[62] A. Nyman, T. G. Zavalis, R. Elger, M. Behm, G. Lindbergh, Analysis of the polarization in a Li-ion battery cell by numerical simulations, J. Electrochemical Soc. 157 (11) (2010) A1236–46.

[63] L. O. Valøen, J. N. Reimers, Transport properties of $LiPF_6$-based Li-ion battery electrolytes, J. Electrochem. Soc. 152 (5) (2005) A882–91.

[64] V. R. Subramanian, V. Boovaragavan, V. Ramadesigan, M. Arabandi, Mathematical model reformulation for lithium-ion battery simulations: Galvanostatic boundary conditions, J. Electrochem. Soc. 156 (4) (2009) A260–71.

[65] L. Cai, R. E. White, Lithium ion cell modeling using orthogonal collocation on finite elements, J. Power Sources 217 (2012) 248–55.

[66] P. W. C. Northrop, V. Ramadesigan, S. De, V. R. Subramanian, Coordinate transformation, orthogonal collocation, model reformulation and simulation of electrochemical-thermal behavior of lithium-ion battery stacks, J. Electrochem. Soc. 158 (12) (2011) A1461–77.

[67] S. Mazumder, J. Lu, Faster-than-real-time simulation of lithium ion batteries with full spatial and temporal resolution, Int. J. Electrochem. 2013 (2013), article ID 268747.

[68] M. Torchio, L. Magni, R. B. Gopaluni, R. D. Braatz, D. M. Raimondo, LIONSIMBA: A Matlab framework based on a finite volume model suitable for Li-ion battery design, simulation, and control, J. Electrochem. Soc. 163 (7) (2016) A1192–205.

[69] A. C. Hindmarsh, P. N. Brown, K. E. Grant, S. L. Lee, R. Serban, D. E. Shumaker, C. S. Woodward, SUNDIALS: Suite of nonlinear and differential/algebraic equation solvers, ACM Trans. Math. Soft. 31 (3) (2005) 363–96.

[70] K. Smith, C.-Y. Wang, Solid-state diffusion limitations on pulse operation of a lithium ion cell for hybrid electric vehicles, J. Power Sources 161 (1) (2006) 628–39.

[71] K. Smith, C. D. Rahn, C.-Y. Wang, Control oriented 1D electrochemical model of lithium ion battery, Energy Convers. Manage. 48 (9) (2007) 2565–78.

[72] C. Rahn, C.-Y. Wang, Battery Systems Engineering, Wiley, New York, 2013.

[73] M. Safari, C. Delacourt, Simulation-based analysis of aging phenomena in a commercial graphite/$LiFePO_4$ cell, J. Electrochem. Soc. 158 (12) (2011) A1436–47.

[74] Y. Xie, J. Li, C. Yuan, Multiphysics modeling of lithium ion battery capacity fading process with solid-electrolyte interphase growth by elementary reaction kinetics, J. Power Sources 248 (2014) 172–9.

[75] T. R. Ashwin, Y. M. Chung, J. Wang, Capacity fade modelling of lithium-ion battery under cyclic loading conditions, J. Power Sources 328 (2016) 586–98.

Nomenclature

Acronyms

1D	One-dimensional
DMC	Dimethyl carbonate
EC	Ethylene carbonate
LAM	Loss of Active Material
LLI	Loss of Lithium Inventory
OCP	Open-circuit potential
P2D	Pseudo-two-dimensional
SEI	Solid/Electrolyte Interface
SOC	State of charge

Greek symbols

β	Bruggeman's exponent
δ	Thickness [μm]
η	Overpotential [V]
κ	Ionic conductivity [S/m]
κ_{SEI}	SEI conductivity [S/m]
λ	Thermal conductivity [W/(m K)]
ϕ	Electrostatic potential [V]
ψ	Cell property
ρ	Mass density [kg/m^3]
σ	Solid-phase conductivity [S/m]
θ	State of charge
ε_f	Filler-phase volume fraction
ε_l	Liquid-phase volume fraction
ε_s	Solid-phase volume fraction

Roman symbols

$\dot{q}$	Heat generation rate [W/m^3]
A	Electrode (transversal) surface area [m^2]
a_s	Active interfacial surface area per unit electrode volume
c_e	Electrolyte phase concentration of lithium ions [mol/m^3]
c_p	Specific isobaric heat capacity [J/(kg K)]
c_s	Solid phase intercalant concentration [mol/m^3]
$c_{s,e}$	Solid phase intercalant surface concentration [mol/m^3]
D	Diffusivity [m^2/s]
E_a	Activation energy [J/mol]
F	Faraday's constant [96487 $\frac{\text{C}}{\text{mol}}$]
$f_\pm$	Mean molar activity coefficient
h	Convective heat transfer coefficient [W/(m^2 K)]
i_0	Exchange current density [A/m^2]
I_a	Applied current [A]
j	Molar flux [mol/(m^2 s)]
k_0	Reaction rate constant [m$^{5/2}$/(mol$^{1/2}$s)]
L	Overall length ($L = \delta_n + \delta_s + \delta_p$) [$\mu$m]
M_{SEI}	SEI molecular mass [kg/mol]
N	Cycle number
q	Capacity [C]
R	Universal gas constant [J/(mol K)]
r	Radial coordinate [m]
R_f	SEI film resistance [Ωm^2]
R_s	Solid particle radius [μm]
T	Temperature [K]
t	Time [s]
t_+^0	Cation transference number
U	Open-circuit potential [V]
x	Spatial coordinate across cell thickness [m]

Subscripts/Superscripts

∞	bulk
a	applied
D	diffusional
dis	discharge
e	electrolyte
f	film; filler phase; final
i	intercalation
l	liquid
n	negative
p	positive
s	side-reaction, solid-phase, separator
eff	effective
max	maximum
ref	reference

Table 1: Thermal properties of materials for the Cai and White [46] cell.

Parameter	Al C.C.	+Electrode ($LiCoO_2$)	Separator	−Electrode (LiC_6)	Cu C.C.
Thickness δ [μm]	10	70	25	73.5	10
Thermal conductivity λ [W/(m K)]	237	2.1	0.16	1.7	401
Mass density ρ [kg/m^3]	2700	2292	1626	5031.67	8940
Isobaric heat capacity c_p [J/(kg K)]	897	750	750	750	385

Table 2: P2D model parameters for the Cai and White [46] cell.

Parameter	+Electrode ($LiCoO_2$)	Separator	-Electrode (LiC_6)
Liquid phase volume fraction ε_l	0.3	0.45	0.4382
Filler phase volume fraction ε_f	0.15	0	0.0566
Solid phase volume fraction ε_s	0.55	-	0.5052
Bruggeman's exponent	1.5	2.3	4.1
Solid phase conductivity σ [S/m]	10	-	100
Solid phase diffusivity D_s [m^2/s]	10^{-11}	-	$5.5\,10^{-14}$
Reaction rate constant k_0 [m$^{5/2}$/(mol$^{1/2}$ s)]	$6.6667\,10^{-11}$	-	$1.764\,10^{-11}$
Particle radius R_s [μm]	8.5	-	12.5
Cation transference number t_+^0	0.435		
Max. solid phase conc. $c_{s,\max}$ [mol/m^3]	51555	-	30556
E_a for solid phase diffusivity [J/mol]	29000	-	58000
E_a for reaction rate constant [J/mol]	58000	-	20000
Initial electrolyte conc. [mol/m^3]	1000		
Initial SOC	0.465	-	0.756
SEI layer initial film resistance R_{SEI} [Ω m^2]	-	-	0.01
SEI layer molar density $\rho_{\text{SEI}}/M_{\text{SEI}}$ [mol/m^3]	-	-	2100
SEI exchange current i_{0s} [A/m^2]	-	-	$8\,10^{-8}$
SEI reference voltage U_s^{ref} [V]	-	-	0.4
SEI layer conductivity κ_{SEI} [S/m]	-	-	$1.7\,10^{-4}$